PAPER • **OPEN ACCESS**

A numerical study of the influence of the choice of rubber material behavior on the static response of tires

A numerical study of the influence of the choice of rubber material behavior on the static response of tires

Baurice Sylvain Sadjiep Tchuigwa[1], Jan Krmela[1,2] and Jan Pokorný[1]

[1] Department of Transport means and Diagnostics, Faculty of Transport Engineering, University of Pardubice, Studentska 95, 532 10 Pardubice, Czech Republic
[2] Faculty of Industrial Technologies in Púchov, Alexander Dubček University of Trenčín, Ivana Krasku 491/30,02001 Púchov, Slovak Republic

E-mail: bauricesylvain.sadjieptchuigwa@student.upce.cz,sylvainsadjiep@gmail.com, jan.krmela@tnuni.sk, jan.pokorny@upce.cz

Abstract. Considering the present-day environmental and energy objectives set forth by governments and aiming at minimizing carbon footprints and fuel consumption in the transportation sector, it is of utmost importance for manufacturers to enhance tire design. This is because doing so has the potential to revolutionize the automotive industry by promoting advancements in structural performance and fuel efficiency while reducing environmental impact and ensuring safer, more dependable vehicle structural performance. Moreover, such an approach has the advantage that the choice of model's features such as the geometry and material mechanical properties, is done in a more detailed manner. The mechanical behavior of rubber compounds used in tire manufacturing has a direct impact on the static as well as the dynamic response of tires in various operating scenarios, such as steady state and transient dynamic. However, in the literature, there is a plethora of works that often consider basic rubber constitutive laws without a consistent study of the impact on the model results. Therefore, this paper proposes a comparative study of the static response of a radial tire using finite element method for different choices of incompressible rubber material behavior ranging from elastic(EL), hyperelastic(HE), visco-hyperelastic(VH) to hyper-pseudoelastic(HM). Simulations of an inflated tire and vertically loaded were conducted in ABAQUS Explicit, and the resulting radial deformation, maximum Von Mixes stress, CPU time, contact patch, and contact pressure were selected as four consistent comparisons. The results show that among the four material cases, the VH and HM material models lead to the most accurate result with a shorter CPU time with the latter. Also, their contact pressure and body stress are higher than those of the elastic and hyperelastic models, and this brings an important solution to the disparity between the calculated and experimentally measured contact pressure in previous works.

Keywords— rubber constitutive law, viscoelastic, hyperelastic, pseudo-hyperelastic, static loading, tire response

1 Introduction

The recent targets in the advancement in the automotive industry have brought to light the urgent need for innovative solutions that promote energy efficiency and environmental sustainability. Among the various elements of a vehicle, tires play a crucial role in determining overall performance, energy consumption, and ecological impact. As a result, enhancing tire models has emerged as a key area of focus for researchers and engineers who are striving to drive these advancements. Improving tire models enables more precise

predictions of tire behavior, leading to substantial improvements in fuel economy, reduced greenhouse gas emissions, and optimized material usage. Therefore, throughout the tire development phases, it is worthwhile to delve into the significance of tire model improvement, emphasizing its potential to transform the automotive sector by fostering advancements in energy efficiency, minimizing environmental impacts, and ensuring safer, more reliable vehicle performance. By refining tire models, the automotive industry can meet the dual challenge of enhancing vehicle performance while adhering to stringent environmental regulations, paving the way for a sustainable and energy-efficient future.

Over the past few years, there has been a significant surge in the interest among researchers and engineers in gaining insight into tire behavior using the Finite element method (FEM) for optimal design, performance, durability, and safety in compliance with government requirements. In the search tool semantic scholar[1], a number of 1620 articles have been recorded on finite element modeling of tires with a significant increase in number observed from 2000. Notwithstanding the fact the worldwide alarming issues of global warming and resource scarcity have been imposed since 2010 up to today, the design of not only resistant tires but also environment-friendlier products using coupling the power of data-driven simulation and advanced simulation techniques during the design process ranging from the product conceptualization phase to prototype validation. Recalling that the FEM is a mathematical technique used to solve partial differential equations, the accuracy of its results depends closely not only on the numerical solver but also on the thorough choice of boundary conditions and material properties. In the realm of tire simulation, different types of material behavior are usually adopted to model the contribution of rubber compounds, which are key elements in tire characteristics in both static and dynamic operating scenarios. While experimental cyclic tensile tests on rubber compounds conducted by authors in [2], [3] reveal that these components typically depict a viso-hyperelastic+Mullins damage response, many authors restricted their model to reduced models such as linear elastic, hyperelastic and visco-hyperelastic.

Andersen [4] designed a laminated linear anisotropic shell-based tire model. Krmela [5] proposed a tire model with orthotropic fiber-reinforced rubber layers for static tire simulation. Mhaske, Narwade, and Nagarkar [6] performed a quasi-static simulation of a passenger tire in LS-DYNA using linear elastic material behavior described solely with the Young moduli E_i and Poisson's ratio ν_i.

Among the hyperelastic-based rubber compound tire models, we can cite the works by Phromjan and Suvanjumrat [7], who selected the Ogden model for quai-static tire finite element tire modeling. Li, Liu, Sun, *et al.* [8] considered a hyperelastic rubber behavior to simulate the impact of tread patterns on the static performance of the tire on a rigid flat surface. Similarly, Fathi, El-Sayegh, Ren, *et al.* [9] adopted a Mooney Rivlin-type hyperelastic rubber constitutive law in their model to simulate tire static performance on a flat rigid surface and dynamic response in the frequency domain in contact rolling with a drum wheel. However, no irreversible material response, such as viscoelasticity, was included in the evaluation of the rolling resistance coefficient. Instead, only parameters external to material behavior, such as inflation pressure, vertical load and rolling speed, were taken into account.

Regarding FEM tire with visco-hyperelastic rubber compound behavior, Srirangam [10] developed the so-called sequentially coupled thermo-mechanical model for tire-road interaction simulation, in which Prony series approach was employed to account for rubber viscosity. Lu, Yang, Wu, *et al.* [11] designed a simplified model with a visco-hyperelastic rubber material response to simulate static and rolling car tires. The accuracy of this approach was estimated at 80 percent after being validated using experimental tests.

Although Mullins's damage is intricately associated with rubber compound response captured experimentally, as mentioned, there is no existing tire simulation inventoried with hyper-pseudoelastic rubber behavior in the literature. So, for the completeness of our comparison, we also consider it in this study. Thereby, in this paper, a dynamic explicit FE-based comparative study is conducted on a static tire using ABAQUS[12] and considering four types of incompressible constitutive laws for rubber compounds: elastic(EL), hyperelastic(HE), visco-hyperelastic(VH) to hyper-pseudoelastic(HM). The selected comparison variables are radial deformation, maximum Von Mixes stress, CPU time, contact patch and contact pressure, respectively.

2 Material and method

Before going further, it is worth defining the hypothesis under which the current study was conducted:

- Rubber compounds, namely tread, inner liner, sidewall, undertread, and apex, are assumed to have the same mechanical behavior so that the unique rubber matrix model holds;
- The rim is modeled as a rigid body using coupling contact with the wheel's center;
- The simplified bead approach with a homogenized property is adopted [13];
- The rigid road model is considered;

- Since only the static vertical loading setup is treated here, frictional effects are disregarded.

2.1 Geometry of the tire:
The geometry of the tire 175/75R14, whose half cross-section is depicted in Fig. 1, was selected for this study and was drawn out from [14]. It is a radial passenger tire with 618mm diameter and 175mm tread width. It is designed to be mounted on a 355.6mm rim diameter.

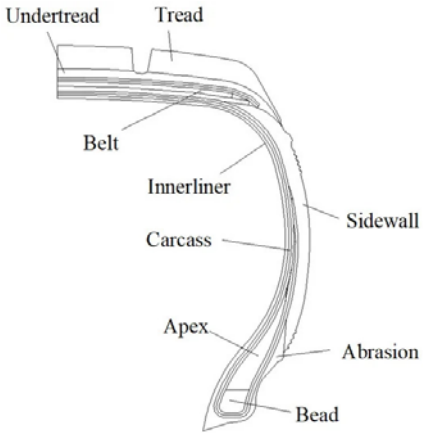

Figure 1: half cross-section of 175/75R14 tire[14]

This scanned image was utilized as a layout to sketch a cross-section in the software AUTOCAD. subsequently, the dxf file was imported into ABAQUS and used to draw the 3D tire using a combination of commands such as revolution, symmetry and mirror. Based on the cross-section in Fig. 2(f), beads in Fig. 2(a) and rubber compounds in Fig. 2(f) were generated from their respective cross-sections using a 360° revolution along the transversal axis passing through the wheel's center(O). As for carcass parts in Fig. 2(d), a single element was first drawn, and the other 299 were generated using a radial pattern feature around the transversal axis.

(a) Beads (b) Steel cords (c) Textile cords

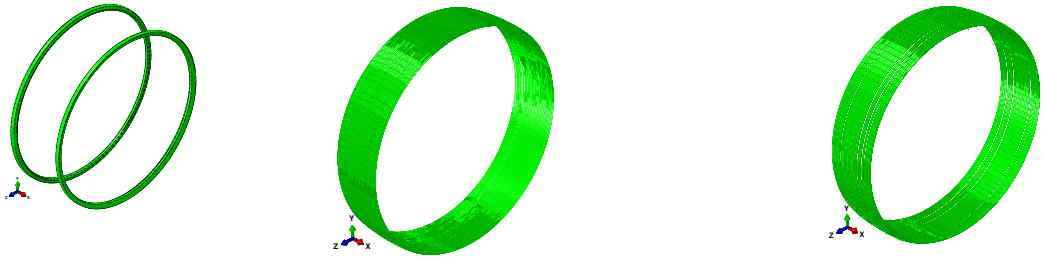

(d) Carcass (e) Cross section of rubber compounds (f) 3D view of rubber compounds

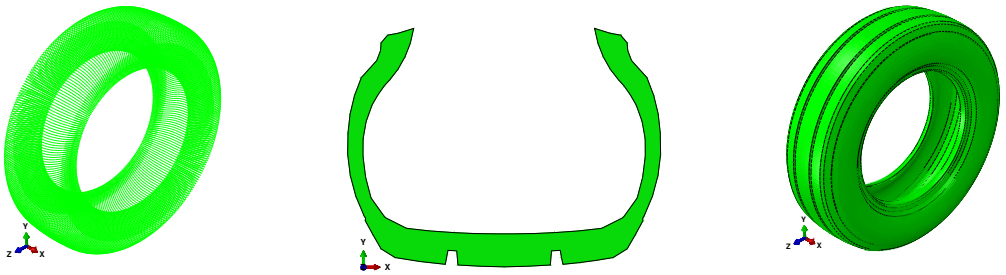

Figure 2: Parts of the tire

2.2 Material properties:
Another important input needed for building the FE model is the mechanical properties of parts or structural components of the problem. For this sake, a combination of uniaxial tensile tests is usually performed in laboratory conditions on steel cords, textile cords, and beads in compliance with the relevant

test standards. Similarly, a cyclic tensile test is needed to capture the dynamic response of rubber compounds as investigated by authors in [15], [16]. Hence, the mechanical properties of the reinforcements adopted in this study are highlighted in Table 1.

Table 1: Reinforcement material propeties

Tire parts	E [MPa]	ν	$\varnothing$ [mm]	ρ [Kg/m^3]
Steel cords	15.724	0.3	0.60	7 850
Textile cords	1900	0.35	0.80	1 250
Carcass	1900	0.40	1.00	1 250
Bead	164499	0.29		7 850

Aside from that, with data extracted from [14], [16], [17], we consider four (04) cases of incompressible rubber material behavior ranging from elastic (EL), hyperelastic (HE), visco-hyperelastic (VH) to hyper-pseudoelastic (HM), all with mechanical properties reported in Table 2

Table 2: Material properties of rubber compounds

Elastic	
Density ρ [Kg/m^3]	1200
E [MPa]	100
ν	0.485

a **Case 1**: linear elastic material model

Hyperelastic	
Density ρ [Kg/m^3]	1200
C_{01} [MPa]	15.724
C_{10} [MPa]	1.111
D_1 [MPa^{-1}]	0.0018

b **Case 2**: Hyperelastic material model

Hyperelastic		viscoelastic	
Density ρ [Kg/m^3]	1200	g_1	0.1433
C_{01} [MPa]	15.724	g_2	0.0852
C_{10} [MPa]	1.111	τ_1 [s]	7.6125
D_1 [MPa^{-1}]	0.0018	τ_2 [s]	235.62

c **Case 3**: Visco-hyperelastic material model

Hyperelastic		Mullins damage	
Density ρ [Kg/m^3]	1200		
C_{01} [MPa]	15.724	r	2.18
C_{10} [MPa]	1.111	m	0.38
D_1 [MPa^{-1}]	0.0018	β	0.5

d **Case 4**: Hyper-pseudoelastic material model

2.3 Mesh properties:

Bearing in mind that the time step in a dynamic explicit scheme is closely conditioned by stable time increment, which in turn depends on mesh properties, special care must be taken when creating the mesh. The best procedure is to mesh each entity separately. Furthermore, it prevents us from ending up with densified mesh in the rubber domain in the vicinity of reinforcements. However, for the sake of reducing the problem size, knowing that the contact zone between the tire and the road is located in the lower portion of the tire throughout the test, the rubber part in Fig. 2(f) was partitioned into two parts: the lower part is bounded by an angle of 35° on either side of the vertical axis centered at O and the second part the remainder. The mesh size of the former part is smaller than that of the latter. Except for beads that were meshed using C3D8R elements, all the other fibers were meshed as B32H elements, which correspond to 1D beam elements (with 3 translations and 3 rotations degrees of freedom per node). Table 3 summarizes the details of the mesh of the tire's parts.

Table 3: Mesh properties

Parts	**Elements**	**Element type**	**Number of elements**
Rubber compounds	3D solid	C3D8R: 8-node linear brick, reduced integration with hourglass control	20 090
Bead	3D solid	C3D8R: 8-node linear brick, reduced integration with hourglass control	3 248
Textile cords	1D beam	B32H: 3-node quadratic hybrid elements	3 082
Carcass	1D beam	B32H: 3-node quadratic hybrid elements	19 800
Steel cords	1D beam	B32H: 3-node quadratic hybrid elements	5 768
Road	2D Shell	S4R: 4-node linear shell with hourglass control	16 950

In addition, enhanced hourglass control together with distortion, was activated to prevent mesh distortion arising from large deformation. Also, reduced integration was selected to avoid volumetric locking, mostly in the rubber part. The created mesh is shown in Fig. 3.

(a) Mesh view on the cross-section (b) Longitudinal view on the tire

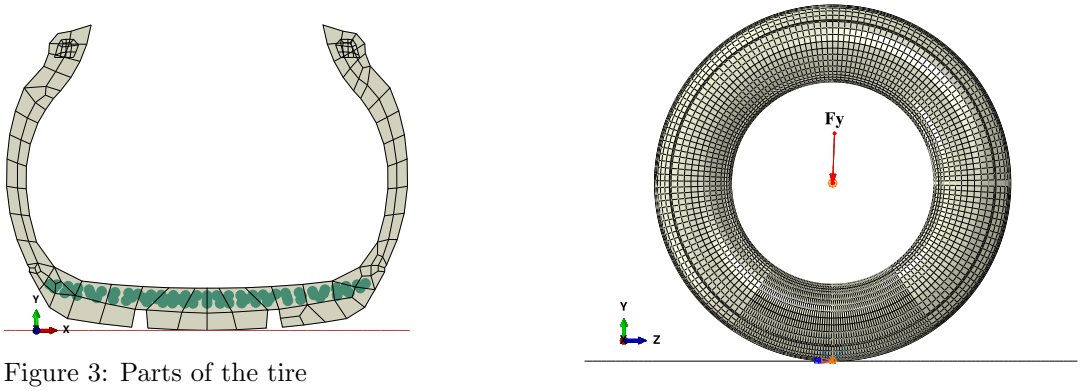

Figure 3: Parts of the tire

2.4 Boundary conditions:
Three types of boundary conditions were enforced: Prior to this, the so-called hard contact type was created.

- *Rim-tire interaction*: As assumed in the introduction, the rim is a rigid body, so we enforce this condition by linking the rim's center (reference point) to its contact zone with the tire through a coupling constraint. To maintain consistency with this concept, we activated kinematic coupling under the coupling window and enabled all degrees of freedom;
- *Tire-road interaction*: This contact constraint was enforced using a combination of general contact interaction and surface-to-surface contact. While the former helps handle contact in general, including self-contact, which prevents contact violations in a body's interaction with itself, the second formulation helps restrict the contacting surface to the specified master (road) and slave (tread outermost face);
- *Embedded constraints*: all fibers, namely carcass, steel cords, textile cords and bead were connected to rubber matrix (hosting domain) using embedded constraints;
- all the degrees of freedom of road's nodes were blocked through the reference point at the center of the road;
- For stability reasons, U_x at the wheel's center was fixed.
- *Vertical applied load* F_y was applied linearly at the reference point located at wheel's center in Fig. 3(b) up to the value of 7500N;
- *Inflation pressure*: a uniformly distributed pressure of 0.35MPa was applied on the inner liner surface;
- *Tire self-weight* was taken into account thanks to gravity effects defined on all model's elements except the road.

The abovementioned loads were applied in a single load step of $1s$, as represented in time history in Fig. 4

(a) gravity in N/Kg (b) Inflation pressure MPa (c) F_y in N

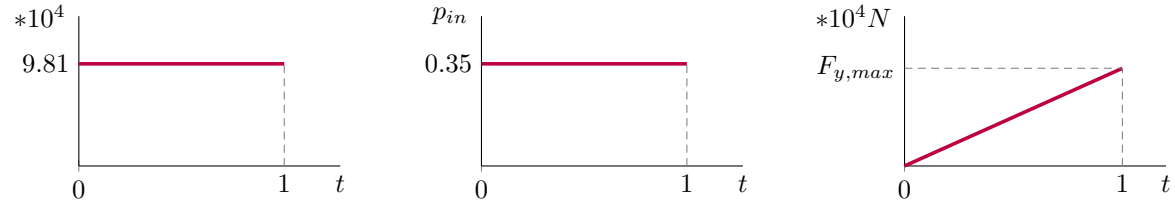

Figure 4: Load definition

2.5 Finite element formulation of problem:
Let $\Omega^{(1)}$ be the bounded domain of space occupied by the tire and $\Omega^{(2)}$ the domain occupied by the road. Let $\partial\Omega_1^{(1)}$, $\Gamma^{(1)}$ and $\partial\Omega_2^{(1)}$ be respectively the inner liner surface, the potential contact surface and the remainder of $\partial\Omega^{(1)}$ such that:

$$\partial\Omega^{(1)} = \partial\Omega_1^{(1)} \cup \partial\Omega_2^{(1)} \cup \Gamma^{(1)} \tag{1}$$

We define the mapping φ that links the position X of $\forall\ M_0 \in \Omega_0^{(i)}$ in the reference configuration to a point $M_t \in \Omega_t^{(i)}$ with position x in the current configuration as follows

$$\begin{array}{c} \varphi : \Omega^{(i)}{}_t \times [0, \mathrm{T}] \longrightarrow \mathbb{R}^3 \\ X \longmapsto x = \varphi(X, t) \end{array} \tag{2}$$

With this definition at hand, we then defined the transformation gradient of the mapping φ

$$\begin{array}{c} F = \dfrac{\partial \varphi}{\partial X} = \dfrac{\partial}{\partial X}\left(X + u\left(X, t\right)\right) \\ F = \boldsymbol{I} + \nabla_X u \quad or \quad F_{\imath J} = \delta_{\imath J} + u_{\imath,J} \end{array} \tag{3}$$

2.5.1 Strong equation :

At every time $t \in [0, T]$, the dynamic response of $\forall\ M_t \in \Omega_t^{(i)}$ in the tire is described by the equilibrium equation given by

$$\nabla \cdot \sigma\left(u\right) + b = \rho \ddot{u}\left(x, t\right) \text{ in } \Omega_t^{(i)} \times [0, T] \tag{4}$$

Where $u \in \mathbb{R}^3$, $u \in \mathbb{R}^3$, $\sigma \in \mathcal{M}^{3\times 3}$ and $b \in \mathbb{R}^3$ are the displacement field, acceleration field, Cauchy stress tensor and body forces, respectively.

2.5.2 Constitutive laws : To Eq. (13), we add the constitutive laws, which depend on the material properties of the domain:
In **linear elasticity**: the stress-strain relationship is described by Hooke's law

$$\sigma = \overline{\overline{\mathcal{C}}} : \varepsilon \tag{5}$$

Where $\overline{\overline{\mathcal{C}}}$ is the material elasticity tensor.
In **Hyperelasticity**: the constitutive equation derives from Mooney Rivlin the strain density given by

$$W\left(\overline{I}_1, \overline{I}_2, J\right) = C_{10}\ \left(\overline{I}_1 - 3\right) + C_{01}\left(\overline{I}_2 - 3\right) + \frac{1}{D_i}(J-1)^2 \tag{6}$$

Where $J = det\left(J\right)$, $\overline{I}_1$ and $\overline{I}_2$ are the determinant jacobean, the reduced form of the first invariant I_1 and the second invariant I_2 of the right Cauchy tensor $C = F^T F$, respectively. C_{ij} and D_1 stand for material constants and compressibility constant. σ is straightforwardly obtained from W the chain rule

$$\sigma\left(t\right) = \frac{1}{J}\frac{\partial W\left(F(t)\right)}{\partial F} F^T \tag{7}$$

In **visco-hyperelasticity**: making use of Prony series, the constitutive equation is given by the convolution equation

$$\begin{cases} \sigma^D\left(t\right) = \sigma_0^D(t) + \displaystyle\int_0^t F_t^{-1}(t-t^{'})\sigma_0^D(t-t^{'})F_t^{-1}(t-t^{'})\dot{g_r}(t^{'})dt^{'} & \text{(8a)} \\ \sigma^H(t) = \sigma_0^H(t) + \displaystyle\int_0^t \sigma_0^H(t-t^{'})\dot{g_r}(t^{'})dt^{'} & \text{(8b)} \end{cases}$$

Where σ_0^D and σ_0^H are the instantaneous deviatoric and hydrostatic stresses, respectively. We recall that the strain energy density function of the material undergoing finite deformation is split into its deviatoric and volumetric components as given in Eq. (6) such that the corresponding stresses can be computed

$$\sigma_0^H(t) = \frac{2}{D_1}(J-1)\ ,\ \sigma_0(t) = \frac{1}{J}\frac{\partial W\left(F(t)\right)}{\partial F} F^T, \sigma_0^D(t) = \sigma_0(t) - \sigma_0^H(t) \tag{9}$$

In **Hyper-pseudoelastic**: the most widely used pseudo-strain energy density function was proposed by Dorfmann and Ogden [18] and reads as

$$\begin{cases} W\left(F, \eta\right) = \eta \hat{W}\left(\overline{F}\right) + \mathcal{U}\left(J\right) + \psi\left(\eta\right) & \text{(10a)} \\ \psi^{'}\left(\eta\right) = -\hat{W}\left(\overline{F}\right) & \text{(10b)} \end{cases}$$

Where η is the damage factor. Ogden and Roxburgh [19] suggested a derivative to $\psi(\eta)$ as a function of the maximum history deviatoric strain density energy $\hat{W}_{max}$ and three other parameters m, β and r as follows

$$\psi^{'}(\eta) = -\left(m + \beta \hat{W}_{max}\right) \mathrm{erf}^{-1}\left(r\left(\eta - 1\right)\right) - \hat{W}_{max} \tag{11}$$

Where erf is the Gauss error function. After replacing Eq. (11) into Eq. (10b) and solving for η, we end up with

$$\eta\left(\overline{F}\right) = 1 - \frac{1}{r}\mathrm{erf}\left(\frac{\hat{W}_{max} - \hat{W}\left(\overline{F}\right)}{m + \beta \hat{W}_{max}}\right) \tag{12}$$

Subsequently, the Cauchy stress can be computed by applying the chain rule

$$\sigma(t) = \frac{1}{J}\frac{\partial W(F, \eta)}{\partial F} F^T \tag{13}$$

2.5.3 Boundary conditions :

The initial conditions prescribed according to test setup are the following:

$$\begin{cases} u(x, 0) = 0 \text{ in } \Gamma^{(2)} \in \Omega^{(2)} & \text{(14a)} \\ \dot{u}(x, 0) = 0 \text{ in } \Omega^{(1)} & \text{(14b)} \end{cases}$$

Aside from initial conditions, we define displacement and traction boundary conditions as follows

$$\begin{cases} u(x, t) = 0 \text{ in } \Gamma^{(2)} \in \Omega^{(2)} & \text{(15a)} \\ \sigma \cdot n = p_{in} \text{ in } \partial\Omega_1^{(1)} & \text{(15b)} \end{cases}$$

Now we define contact conditions between $\Gamma^{(1)}$ and $\Gamma^{(2)}$ using Karush-Kuhn-Tucker (KKT) conditions

$$g_N(X, t) \geq 0,\ p_N(X, t) \leqslant 0,\ p_N(X, t)\, g_N(X, t) = 0 \tag{16}$$

Where p_N and g_N are the normal contact pressure and the gap function. The latter is given by the expression

$$g_N(X, t) = \vec{n}_1 \cdot \left[x^{(1)}(X^{(1)}, t) - x^{(2)}(X_c^{(2)}, t]\right] \geq 0 \tag{17}$$

Having all the ingredients at hand, we now proceed with the variational formulation. Let V_h be the space of kinematically admissible displacements associated with Ω_h. The variational formulation of the problem is defined in the discretized space by find $u_h \in V_h$ and $p_N \in V_p$ such that :

$$\int_{\Omega_h^{(1)}} \rho \ddot{u}_h \cdot \delta u_h dV + \int_{\Omega_h^{(1)}} \sigma_h : \delta\varepsilon_h dV = \int_{\Omega_h^{(1)}} b \cdot \delta u_h dV + \int_{\partial\Omega_h^{(1)}} p_{in} \cdot \delta u_h dS - \int_{\partial\Omega_h^{(1)}} p_N \cdot \delta g_N dS \tag{18a}$$

$$\int_{\partial\Omega_h^{(1)}} \delta p_N \cdot g_N dS = 0 \tag{18b}$$

After writing out Eq. (19), considering constitutive laws for different case in Sect. 2.5.2, we end up with the discrete equation of motion given by

$$M\ddot{u}(t) + C\dot{u}(t) + Ku(t) = f_{ext}(t) - f_{contact}(t) \tag{19a}$$

$$\delta W(u, t, p_N) = 0 \tag{19b}$$

Where M, C, K, f_{ext}, and $f_{contact}$ are the mass matrix, damping matrix, stiffness matrix, external force vector, and contact force vector, respectively. The reader can find further details on these expressions in [20]. With the help of a dynamic explicit scheme, it is possible to solve this equation without strictly enforcing equilibrium like in the implicit scheme through Newton-Raphson algorithm. Therefore, the former method is faster, but its drawback is that it necessitates choosing a stable time step Δt that fulfills the stability condition given as

$$\Delta t_{stable} = \frac{h}{c_L} \tag{20}$$

where h is the characteristic length of the element and $c_L = \sqrt{\frac{E}{\rho}}$. An alternative to this approach defined the critical time step as a function of the maximal eigenfrequency of the mesh and reads as follows

$$\Delta t_{stable} \leq \frac{2}{\omega_{max}} \tag{21}$$

Depending on the size of the finite elements, Δt_{stable} can be very small and lead to very long execution times. For the sake of getting the highest value possible, hexahedral elements were chosen over tetrahedral elements, and the mesh feature was set to comply with contact conditions and stability reasons. Under the details provided in Table 3, an initial time increment of $\Delta t_{stable} = 1.0128 \times 10^{-6} s$ was obtained. Among possible acceleration strategies, mass scaling is considered here to increase the time step. So, after many stability verifications, we obtained an acceptable mass scaling factor of 100, which means that in virtue of Eq. (20), we ended up with $\Delta t = 1.0128 \times 10^{-5} s$.

3 Results and discussion

All of the four tire models with rubber compounds outlined in Table 2, were computed separately, and the corresponding distribution of Mixes stress, vertical displacement U_y and normal contact stress are presented below in Fig. 5, 6, 7, 8, Fig. 9, 10, 11, 12 and Fig. 13, respectively.

3.1 Von Mises stress distribution in [MPa]

(a) 3D view (b) rear view

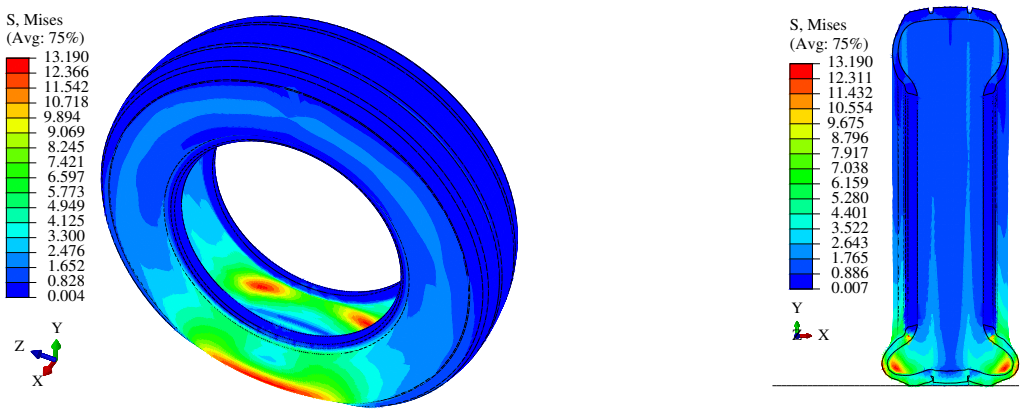

Figure 5: σ_{VM} at $t = 1\ s$ in the tire with **incompressible linear elastic** rubber materials.

(a) 3D view (b) rear view

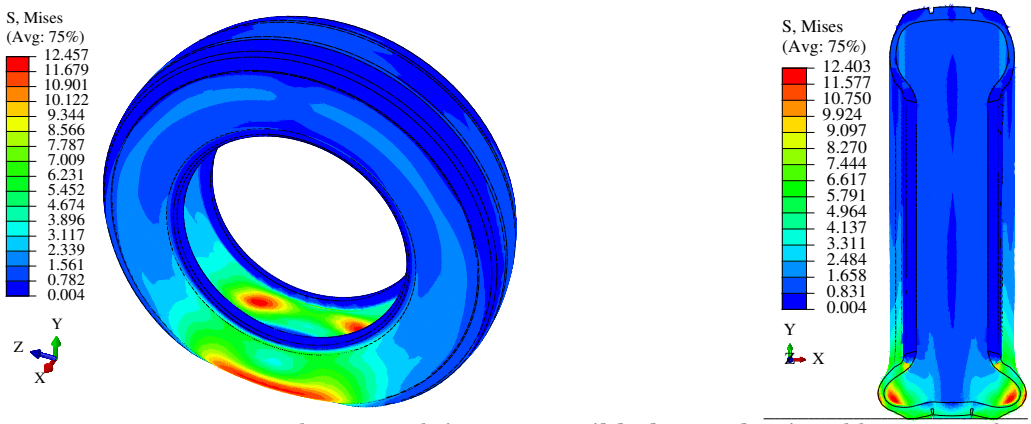

Figure 6: σ_{VM} at $t = 1\ s$ in the tire with **incompressible hyperelastic** rubber materials.

(a) 3D view (b) rear view

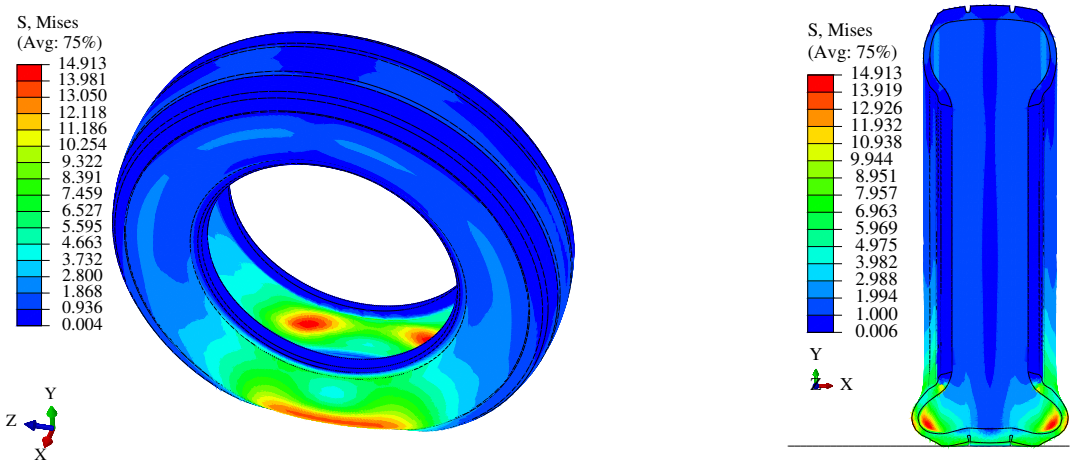

Figure 7: σ_{VM} at $t = 1\ s$ in the tire with **incompressible visco-hyperelastic** rubber materials.

(a) 3D view (b) rear view

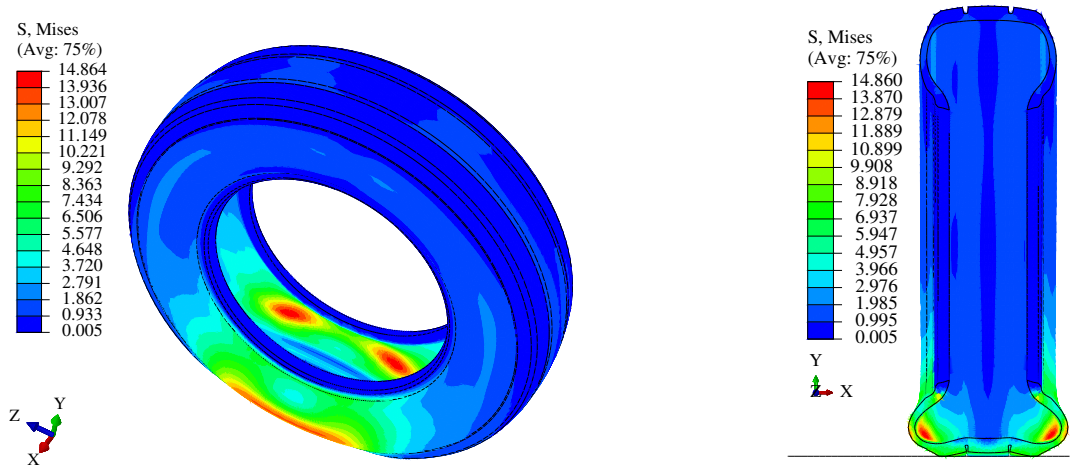

Figure 8: σ_{VM} at $t = 1\ s$ in the tire with **incompressible hyper-pseudoelastic** rubber materials.

As expected, we observe that Von Mises stress is not the same for all the models, of which the values of the visco-hyperelastic and hyper-pseudoelastic models are closer to each other. The hyperelastic model has the lowest values and is followed by the elastic model.

3.2 Distribution of the vertical displacement U_y in [mm]

(a) 3D view (b) rear view

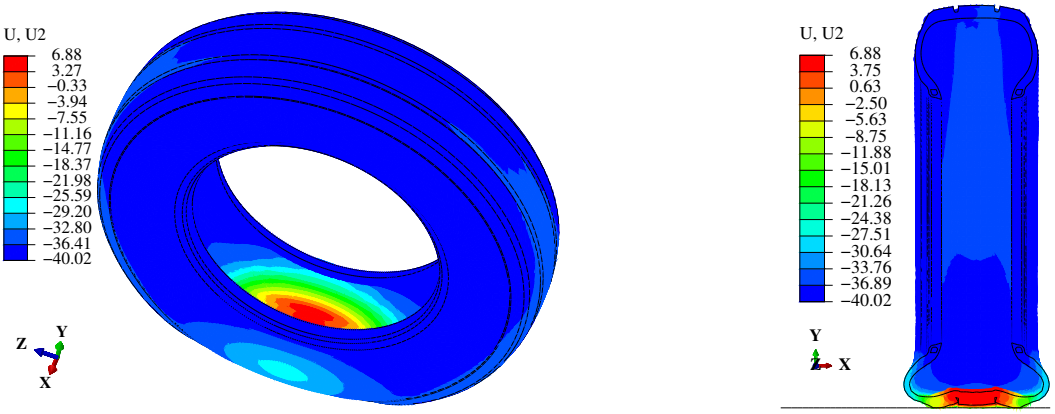

Figure 9: $U_Y(in\ mm)$ at $t = 1\ s$ in the tire with **incompressible linear elastic** rubber materials.

(a) 3D view (b) rear view

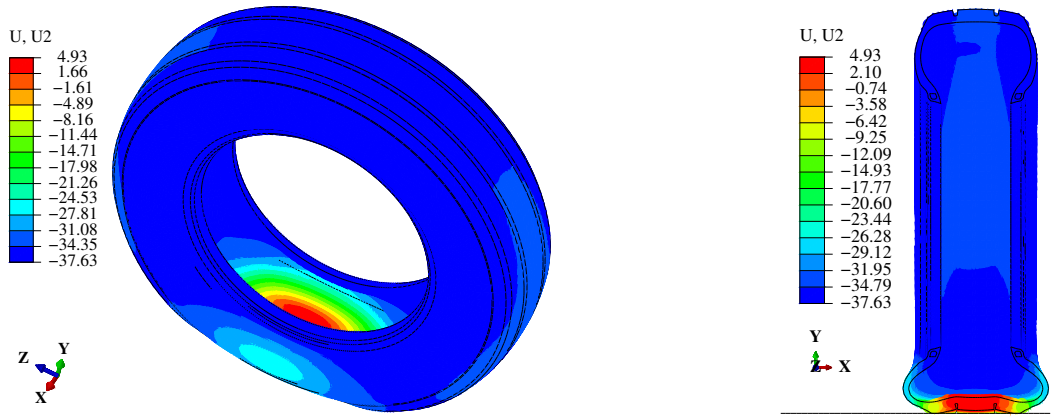

Figure 10: $U_Y(in\ mm)$ at $t = 1\ s$ in the tire with **incompressible hyperelastic** rubber materials.

(a) 3D view (b) rear view

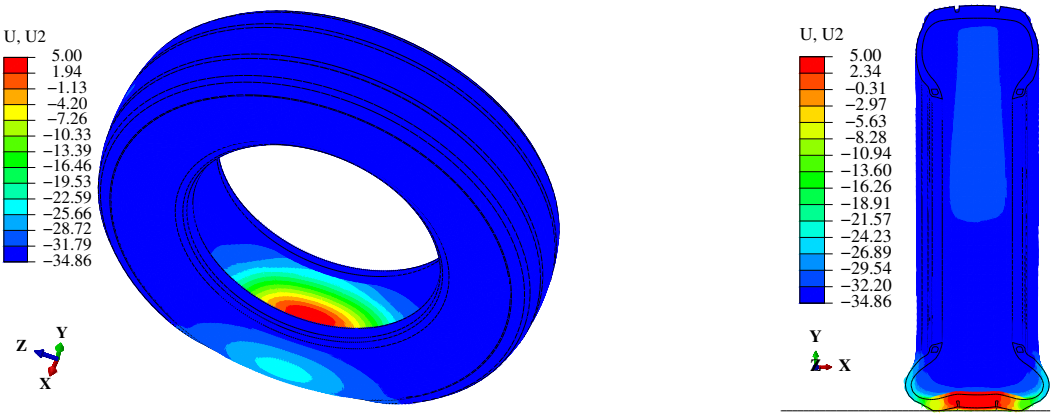

Figure 11: $U_Y(in\ mm)$ at $t = 1\ s$ in the tire with **incompressible visco-hyperelastic** rubber materials.

(a) 3D view (b) rear view

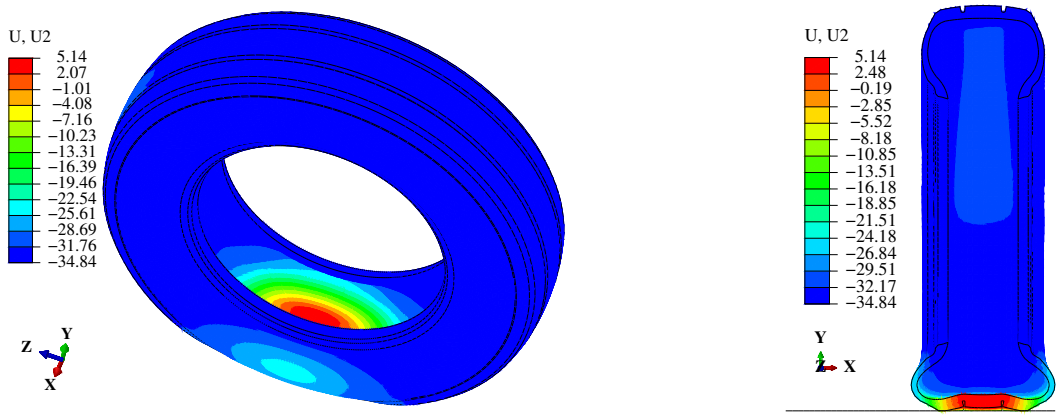

Figure 12: $U_Y(in\ mm)$ at $t = 1\ s$ in the tire with **incompressible hyper-pseudoelastic** rubber materials.

When it comes to the comparison of vertical displacement U_y, we observe that the elastic model witnesses the highest vertical deformation $U_y = 40.019mm$ and is followed by the hyperelastic model with $U_y = 37.857mm$. After the previous ones, the visco-hyperelastic and hyper-pseudoelastic models come with almost the same value of U_y.

3.3 Distribution of the normal contact stress p_N in [MPa]

(a) Elastic (b) Hyperelastic (c) Visco-hyperelastic (d) Hyper-pseudoelastic

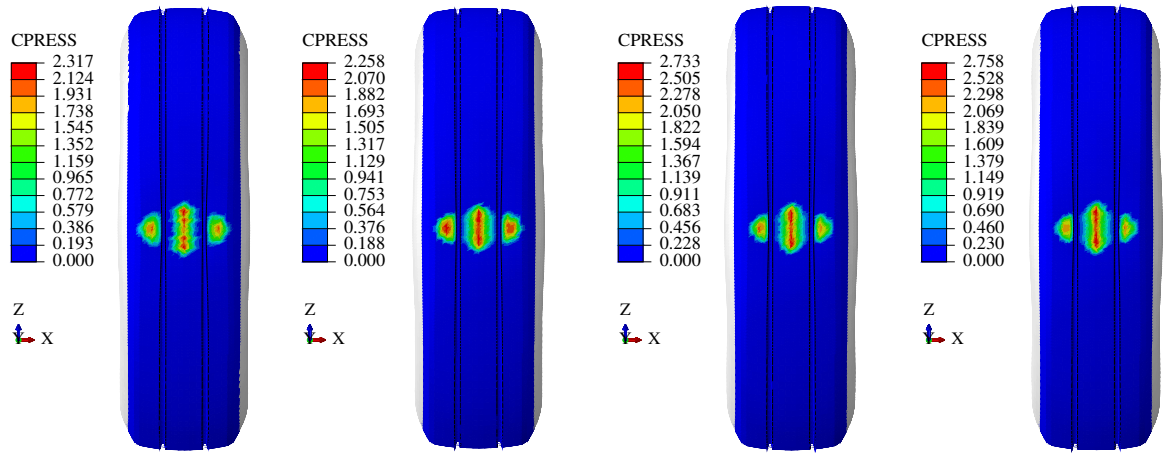

Figure 13: Normal contact stress p_n at $t = 0.46\ s$ for different rubber material constitutive laws.

We see that, for instance, at $t = 0.46$, the contact patch shape is nearly the same for all models. However, there is a higher normal contact stress (circa 18%) with the visco-hyperelastic and hyper-pseudoelastic models than the elastic model.

3.4 Comparison of results

At the end of the simulation, we collected σ_{VM}, U_y, p_N and $CPU\ time$ for all of the four models and summarized them in Table 4 below

Table 4: results and performance

Model	**Elastic**	**Hyperelastic**	**Visco-hyperelastic**	**Pseudo-hyperelastic**
σ_{VM} [MPa]	13.190	12.460	14.910	14.864
U_y [mm]	40.02	37.63	34.86	34.65
p_N [MPa]	6.783	9.502	11.230	11.385
$CPU\ time$ [min]	82.00	70.53	100.30	68.82

It is more convenient to compare these models using a bar chart of the data in Table 4 and depicted in Fig. 14

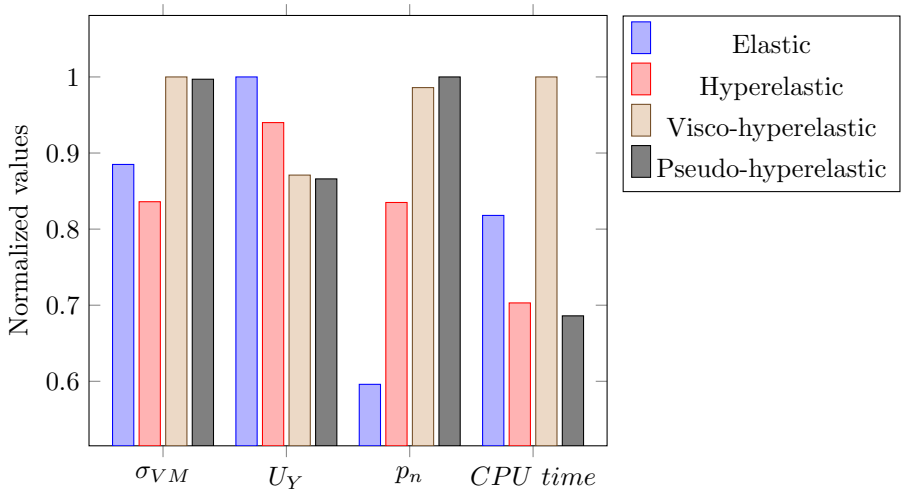

Figure 14: Performance analysis of the different models

4 Conclusion

This study has explored different approaches to modeling static tire response using different rubber constitutive behaviors, including elastic, hyperelastic, visco-hyperelastic, and unexplored hyper-pseudoelastic rubber behaviors. The comparative analysis was conducted on the results obtained using dynamic explicit FEM in ABAQUS, taking into account tire performance metrics such as radial deformation, maximum Von Mises stress, contact patch, and contact pressure. In light of the findings of this study, we demonstrate that the choice of rubber compound material behavior has to be made judiciously in accordance with the real material response recorded in laboratory testing so as to mimic the mechanical contribution of the element in the FE model. In such a way, there should be a good tradeoff between computational complexity and model accuracy. So, as long as the vertical displacement is the only target of the study, the visco-hyperelastic suffices, but when extended results such as stress distribution, contact pressure and CPU time are concerned, the model with Hyper-pseudoelastic rubber compound has to be prioritized. Furthermore, this model is better than the others since it is computationally less intensive and gives better results. The knowledge gained in this study paves the way for a more in-depth consideration of the constitutive behavior of rubber compounds for more accurate prediction of tire response, which is essential for the optimal use of materials but also for improving tire energy performance. In future work, we will conduct a comparison analysis of the same tire in frictional rolling conditions with thermo-mechanical loads and provide the field with further recommendations on the choice of rubber compound material behavior.

Acknowledgement

The authors acknowledge the funding provided by the University of Pardubice through the grant number SGS 2024. This research work had been supported by University of Pardubice grant number SGS 2024 and the Cultural and Educational Grant Agency of the Slovak Republic (KEGA), project No. KEGA 003TnUAD-4/2022 “Simulation of basic and specific experiments of polymers and composites based on experimental data in order to create a virtual computational-experimental laboratory of mechanical tests”.

Statements and Declarations

Conflicts of Interest: The authors declare no conflict of interest.

References

[1] S. Scholar, *Semantic scholar*, `http://web.archive.org/web/20080207010024/http://www.808multimedia.com/winnt/kernel.htm`, Accessed: 15-04-2024.

[2] J. Krmela, M. Michna, Z. Růžička, V. Krmelová, and A. Artyukhov, "Cyclic Testing of Polymer Composites and Textile Cords for Tires," *Polymers*, vol. 15, no. 10, pp. 1–15, 2023, ISSN: 20734360. DOI: 10.3390/polym15102358.

[3] B. Fazekas and T. J. Goda, "Constitutive modelling of rubbers: Mullins effect, residual strain, time-temperature dependence," *International Journal of Mechanical Sciences*, vol. 210, 2021, ISSN: 00207403. DOI: 10.1016/j.ijmecsci.2021.106735.

[4] C. M. Andersen, "Deep anistropic shell program for tire analysis," NASA, Tech. Rep., 1981.

[5] J. Krmela, "The computational modelling of tire," vol. Vol. 10, no. 3(27), Nov. 2009.

[6] M. P. Mhaske, P. Narwade, and M. Nagarkar, "Analysis of vertical stiffness of passenger car tire at different pressure using fe model," *International Journal of Innovations in Engineering Research and Technology*, pp. 1–6, 2015.

[7] J. Phromjan and C. Suvanjumrat, "A suitable constitutive model for solid tire analysis under quasi-static loads using finite element method," *Engineering Journal*, vol. 22, pp. 141–155, Mar. 2018. DOI: 10.4186/ej.2018.22.2.141.

[8] Y. Li, C. Liu, Y. Sun, Y. Li, C. Xu, and M. Xie, "Modeling Methods and Simulation Analysis of Radial Tire with Different Tread Patterns," vol. 9, no. 1, pp. 20–30, 2020.

[9] H. Fathi, Z. El-Sayegh, J. Ren, and M. El-Gindy, "Modeling and validation of a passenger car tire using finite element analysis," *Vehicles*, vol. 6, no. 1, pp. 384–402, 2024, ISSN: 2624-8921. DOI: 10.3390/vehicles6010016. [Online]. Available: https://www.mdpi.com/2624-8921/6/1/16.

[10] S. Srirangam, "Numerical simulation of tire-pavement interaction," English, Dissertation (TU Delft), Delft University of Technology, 2015, ISBN: 978-94-6203-873-8. DOI: 10.4233/uuid:ccf73339-112f-4fff-b846-a828a6120a3d.

[11] D. Lu, W. Yang, H. Wu, and T. Zhou, "Research on simplified tire finite element modeling and simulation method," *Proceedings of the Institution of Mechanical Engineers, Part D: Journal of Automobile Engineering*, 2023. DOI: 10.1177/09544070231207528. [Online]. Available: https://doi.org/10.1177/09544070231207528.

[12] Dassault Systemes Simulia Corpia Corp, *ABAQUS/Standard User's Manual, Version 6.9*, 2020.

[13] Y. Li, X. Sun, J. Song, S. Zhang, and S. Han, "Topological structure and experimental investigation of a novel whole tire bead," *Materials Design*, vol. 203, p. 109 592, 2021, ISSN: 0264-1275. DOI: https://doi.org/10.1016/j.matdes.2021.109592.

[14] G. Wang, W. Wang, C. Liang, and L. Cao, "Fatigue life prediction of radial tire bead using a maximum strain energy density range method," *Applied Sciences*, vol. 11, no. 12, p. 5477, 2021, ISSN: 2076-3417. DOI: 10.3390/app11125477. [Online]. Available: https://www.mdpi.com/2076-3417/11/12/5477.

[15] B. Fazekas and T. J. Goda, "Closed-form and numerical stress solution-based parameter identification for incompressible hyper-viscoelastic solids subjected to various loading modes," *International Journal of Mechanical Sciences*, vol. 151, pp. 650–660, Feb. 2019, ISSN: 00207403. DOI: 10.1016/j.ijmecsci.2018.12.011. [Online]. Available: https://linkinghub.elsevier.com/retrieve/pii/S0020740318335781.

[16] B. Fazekas and T. J. Goda, "Constitutive modelling of rubbers: Mullins effect, residual strain, time-temperature dependence," *International Journal of Mechanical Sciences*, vol. 210, p. 106 735, Nov. 2021, ISSN: 00207403. DOI: 10.1016/j.ijmecsci.2021.106735. [Online]. Available: https://linkinghub.elsevier.com/retrieve/pii/S0020740321004665.

[17] J. Krmela, *Experiments and computational modelling of tires: Textbooks for university students*, Zborov, Czech Republic, 2020.

[18] A. Dorfmann and R. Ogden, "A constitutive model for the Mullins effect with permanent set in particle-reinforced rubber," *International Journal of Solids and Structures*, vol. 41, no. 7, pp. 1855–1878, Apr. 2004, ISSN: 00207683. DOI: 10.1016/j.ijsolstr.2003.11.014. [Online]. Available: https://linkinghub.elsevier.com/retrieve/pii/S0020768303006504.

[19] R. W. Ogden and D. G. Roxburgh, "A pseudo–elastic model for the Mullins effect in filled rubber," *Proceedings of the Royal Society of London. Series A: Mathematical, Physical and Engineering Sciences*, vol. 455, no. 1988, pp. 2861–2877, Aug. 1999, ISSN: 1364-5021. DOI: 10.1098/rspa.1999.0431. [Online]. Available: https://royalsocietypublishing.org/doi/10.1098/rspa.1999.0431.

[20] P. Wriggers, *Nonlinear finite element methods*. Springer Berlin, Heidelberg, 2008, p. 572. DOI: 10.1007/978-3-540-71001-1.